Title

Size-controlled assembly of phase separated protein condensates with interfacial protein cages.

Permalink

Journal

Authors

Oh, Hyeok
Lee, Yongsuk
Hwang, Haerang
et al.

Publication Date

DOI

Article

Size-controlled assembly of phase separated protein condensates with interfacial protein cages

Hyeok Jin Oh [1,2], Yongsuk Lee [1,2], Haerang Hwang[1], Kibeom Hong [1], Hyeongjoo Choi[1], Jin Young Kang [1] & Yongwon Jung [1] ✉

Phase separation of specific proteins into liquid-like condensates is a key mechanism for forming membrane-less organelles, which organize diverse cellular processes in space and time. These protein condensates hold immense potential as biomaterials capable of containing specific sets of biomolecules with high densities and dynamic liquid properties. Despite their appeal, methods to manipulate protein condensate materials remain largely unexplored. Here, we present a one-pot assembly method to assemble coalescence-resistant protein condensates, ranging from a few μm to 100 nm in sizes, with surface-stabilizing protein cages. We discover that large protein cages (~30 nm), finely tuned to interact with condensates, efficiently localize on condensate surfaces and prevent the merging (coalescence) of condensates during phase separation. We precisely control condensate diameters by modulating condensate/cage ratios. In addition, the 3D structures of intact protein condensates with interfacial cages are visualized with cryo-electron tomography (ET). This work offers a versatile platform for designing size-controlled, surface-engineered protein condensate materials.

Liquid-liquid phase separation (LLPS) of specific proteins into highly dense liquid droplets has emerged as a key mechanism for the formation of membrane-less organelles (MLOs), which play a crucial role in temporally and spatially coordinating diverse biochemical processes within cells[1–3]. Protein LLPS is driven by weak, multivalent interactions, leading to the spontaneous clustering of proteins into condensed assembly structures[4]. These protein condensates exhibit dynamic liquid properties, including the ability to exchange with the surrounding environment, undergo fusion events, recruit specific biomolecules, and disassemble as needed[5]. This dynamic behavior allows protein condensates to serve as specialized micro-compartmental hubs, enriched with specific biomolecules, to dynamically regulate cellular activities[6].

Beyond their essential functions in cells, protein condensates are compelling candidates for biomaterials distinguished by features[7]. A specific set of biomolecules can be reversibly packed within confined spaces at high densities under physiological conditions. The liquid nature provides a dynamic platform with the potential to allow and control communications with outside materials. Additionally, through the manipulation of protein composition or adjustment of environmental conditions, researchers can engineer protein condensates with tailored characteristics[8]. Moreover, serving effectively as MLOs, protein condensates can act as ideal compartmental reactors for diverse biomolecular processes. Several recent studies have showcased the versatility of these protein condensate materials, demonstrating their utility as core backbones for artificial cells[9,10], delivery vesicles for drugs[11,12], and reactors for biochemical reactions[13,14].

While protein condensate materials hold significant promise, the assembly of stable protein condensates with defined size and enduring structural integrity remains a largely unexplored challenge. The formation of protein condensates through LLPS involves continuous nucleation, growth, and fusion (coalescence) processes, leading to

[1]Department of Chemistry, Korea Advanced Institute of Science and Technology, Daejeon, Republic of Korea. [2]These authors contributed equally: Hyeok Jin Oh, Yongsuk Lee. ✉e-mail: ywjung@kaist.ac.kr

intrinsic size fluctuations[4,15,16]. In particular, the continuous coalescence of multiple protein condensates into larger condensates presents a significant obstacle to achieving reliable protein condensate assembly. Additionally, the fluidic architecture and rather sticky surfaces (with high protein content) of protein condensates make it challenging to maintain condensate structure during various synthesis steps. Complicating matters further, the diverse physical properties and LLPS propensities exhibited by different types of condensates hinder the development of universally applicable assembly strategies.

Employing a physical barrier on the surface has proven to be the most effective strategy for stabilizing inherently unstable colloidal structures[17]. Amphiphilic surfactants, commonly employed in the synthesis of colloidal micro/nano materials, have been instrumental in mediating interactions between two immiscible components, such as nanoparticles and solvents or water and oil[18,19]. However, the less clear immiscibility between aqueous solutions and protein condensates poses a challenge in designing effective surface-stabilizing agents. A recent study reported the successful engineering of an amphiphilic protein surfactant that hindered the coalescence of protein condensates[20,21]. Still, robust surface-stabilizing methods are required to effectively interrupt protein condensate formation processes and produce condensates with a wide and defined range of sizes.

Beyond amphiphilic surfactants, symmetric small particles offer an alternative for stabilizing colloidal structures, particularly liquidic emulsions, by adsorbing onto the unstable emulsion interface[22]. The stability of these so-called Pickering emulsions can be tuned by adjusting the size and surface binding affinity of the stabilizing particles, referred to as Pickering agents[23–25]. The concept of Pickering emulsions, which does not necessitate amphiphilicity, holds great promise for the stable assembly of liquidic protein condensates. Indeed, recent studies have reported that certain protein clusters and RNA exhibit Pickering agent-like features, binding to condensate surfaces and impeding condensate coalescence in cells[26,27]. Here, we report a generally applicable method to assemble stable, coalescence-prevented protein condensates with sizes ranging from a few micrometers down to 100 nanometers by employing interfacial protein cages. Multiple protein cages were engineered as surface stabilizers, and their interactions with condensate surfaces were precisely tuned to produce diverse types of cage-stabilized protein condensates. Precise control over condensate sizes was achieved by adjusting the relative quantities of condensate-forming proteins and interfacial cages, while the resulting condensates retained all dynamic liquid properties. Structural features of condensates with surface protein cages were visualized using cryo-ET.

Results

Assembly of protein cage-stabilized protein condensates

According to Pickering emulsion theory, the energy required to displace a Pickering particle agent from the emulsion interface depends on the particle's radius and its relative affinities toward both phases, such as oil and water[28,29]. Larger particles, possessing a greater contact area and adsorption energy, contribute to enhanced surface stabilization. Likewise, maximum energy stabilization occurs when Pickering agents show similar affinities towards both phases. In contrast to emulsions formed with two chemically distinct phases (e.g., oil and water), protein condensates consist of two aqueous phases differing only in protein concentration. We envisioned that the surface stabilization of protein condensates will be primarily influenced by the interaction of interfacial agents with condensate-forming proteins, particularly in the dense condensate phase (Fig. 1a). To develop ideal Pickering agent-like surface stabilizers for protein condensates, we explored protein cages with diverse diameters ranging from 10 to 40 nm. Protein cages offer highly uniform sizes, and, more importantly, their interactions with protein condensates can be thoroughly tuned by precise cage engineering.

Protein condensates were prepared using a previously developed metal ion-induced LLPS protocol[30]. Phase-separable proteins, tagged with six His residues (6His), can be clustered by Ni^{2+}, where a Ni^{2+} ion is coordinated by two (or more) 6His tags[31], leading to subsequent phase separation. Various protein condensates with different properties, such as rigidity, can be formed by switching phase-separable proteins[30]. Moreover, 6His can also be fused to protein cages to mediate interactions between cages and condensates through Ni^{2+}-6His coordination. The strength of this interaction can be further varied by Ni^{2+} concentrations. Initially, rigid and positively charged protein condensates were prepared using a proline-rich motif (PRM) and its binding domain SH3 (PRM-SH3-6His, PSH)[30]. Fluorescence recovery after photobleaching (FRAP) images indicated the highly rigid nature of PSH condensates (Fig. 1b). PSH condensate droplets were formed by simply mixing PSH and Ni^{2+}. For interfacial protein cages, three cages with different sizes and oligomeric states were engineered: octameric isoaspartyl dipeptidase (POK, ~10 nm)[32], 24-meric human ferritin (HF, ~15 nm)[33], and 60-meric artificial cage mi3 (~25 nm)[34] (Fig. 1c and Supplementary Fig. 1). Negatively charged GFP was uniformly introduced on all protein cage surfaces to induce the cage's electrostatic binding to positively charged PSH condensates with similar charge densities but with different sizes. Protein cages were prepared also with and without 6His. Additionally, to further increase cage particle size, we assembled multiple ferritins into a spherical structure (HF oligo, ~40 nm), as previously reported[35]. In HF oligo, a single GFP-fused HF is surrounded by 4–5 HF cages via leucine zipper binding, and only the core GFP-fused HF is modified with 6His (Supplementary Fig. 1c).

We first examined interactions between protein cages and pre-formed PSH condensates. Protein cages were introduced to PSH condensates 2 min after LLPS induction (final [cage] = 50 μg/mL, [PSH] = 500 μg/mL), and both dye-labeled condensates (Cy5, magenta) and GFP-fused cages (green) were imaged after 10 and 60 min of incubation (Fig. 1d). In the absence of protein cages, the size of PSH condensate droplets increased over time, up to ~4 μm, likely through condensate coalescence. All (negatively charged) protein cages, as well as control monomeric GFP, strongly adsorbed on (positively charged) PSH condensate surfaces, with the presence of 6His on cages further enhancing this adsorption. The highly dense and rigid structure of PSH condensates might impede further penetration of cages[30]. Despite robust surface binding, HF and POK cages could not prevent condensate coalescence, resulting in condensate growth similar to that observed in free condensates. Interestingly, however, with larger HF oligo and mi3 cages, condensate sizes and morphologies are nearly identical both at 10 min and 60 min, indicating potent surface stabilization and inhibition of coalescence. Time-course analysis revealed that uncaged PSH condensates consistently fused upon contact, whereas mi3-stabilized PSH condensates rarely fused, sometimes remaining in contact for a period before eventually detaching (Supplementary Fig. 2a and Supplementary Video 1). These findings show the promising potential of properly engineered protein cages as effective stabilizers for protein condensates.

While generated PSH condensates could be effectively stabilized by proper protein cage adsorption, controlling condensate size remained a challenging task. To regulate condensate size, rapidly growing and easily fusing condensates must be trapped and stabilized through cage adsorption. However, the growing kinetics of protein condensates remain largely unexplored, and trapping condensates at the early LLPS stage, especially for smaller condensate assembly, presents huge practical challenges. Therefore, we induced PSH LLPS in the presence of cages (one-pot) to engage in condensate formation from the initiation of LLPS in a more equilibrated manner. All protein cages with 6His, except HF oligo, which has only partially exposed 6His tags (Supplementary Fig. 1c), were observed inside condensates rather than on surfaces and did not prevent condensate growth (Fig. 1e). The
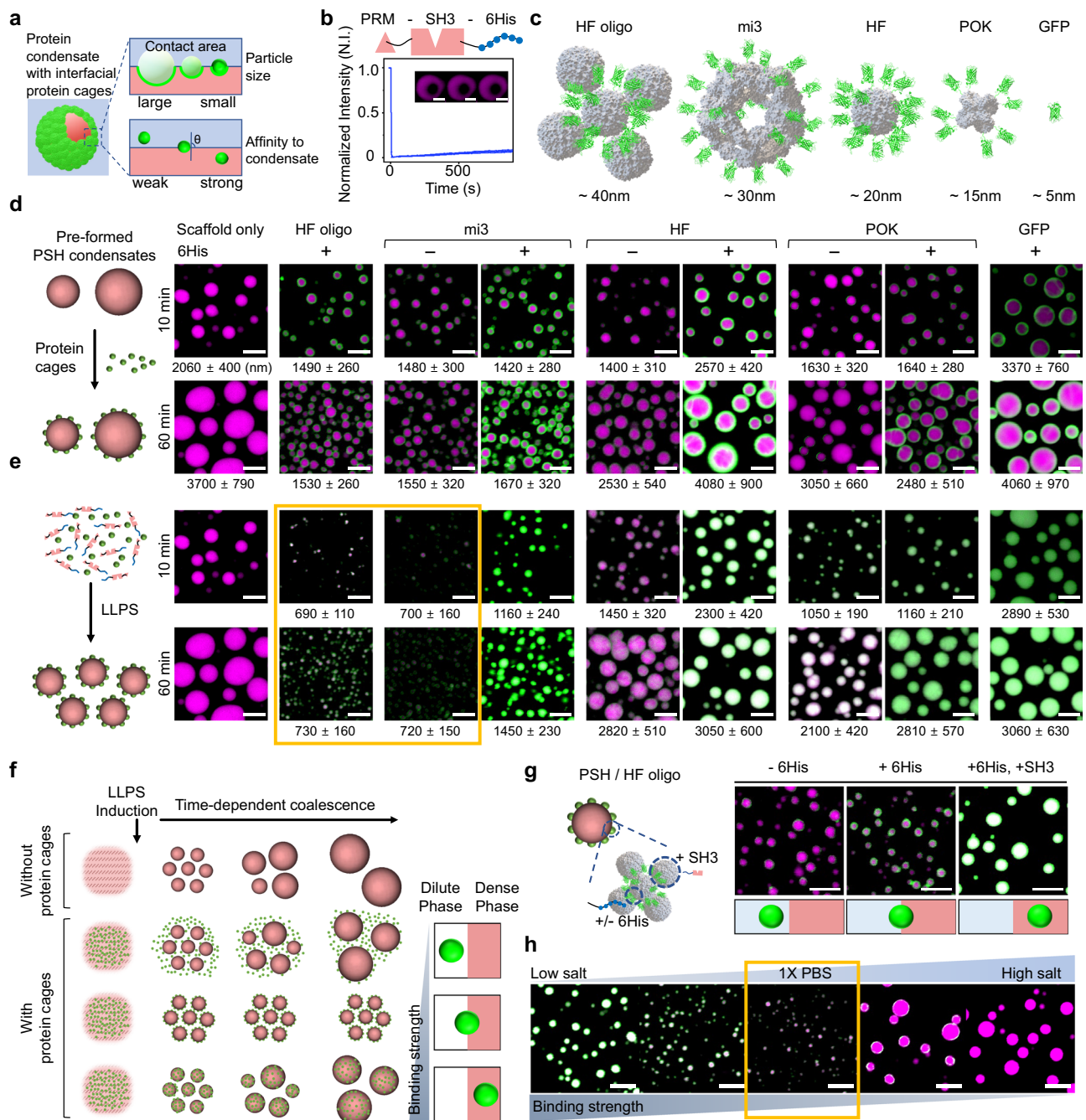
Fig. 1 | Assembly of surface-stabilized protein condensates with interfacial protein cages. a Schematic diagram of surface-stabilized (coalescence-inhibited) protein condensates with interfacial protein cages featuring optimized cage size and affinity to condensates. **b** FRAP recovery profile ($n = 10$ condensates) and confocal images of bleached PSH (magenta) condensates. **c** Schematic structures of designed GFP (green)-fused interfacial protein cages. The approximate size of each cage is indicated below. **d** Sequential introduction (schematically expressed left) of HF oligo, mi3, HF, POK, and monomeric GFP with (+) or without (−) 6His to pre-formed PSH condensates. Confocal images of PSH condensates (magenta) without (scaffold only) or with added protein cages (green) after 10- and 60-min incubations are presented with average diameters shown below images. **e** Confocal images of PSH condensates (magenta) phase separated in the presence of protein cages (one-pot assembly) with average diameters. Surface-stabilized (coalescence-inhibited) protein condensate images are indicated with a yellow box. **f** Schematics of the assembly principles of surface-stabilized protein condensates with interfacial protein cages, depending on cage-condensate binding strengths. **g** Binding strength variation between HF oligo and PSH by removing 6His (weaker) or adding SH3 (stronger) for HF oligo. Confocal images of PSH condensates with HF oligo variants are presented. **h** Confocal images of mi3-treated PSH condensates at different salt concentrations. Optimally stabilized condensates are indicated with a yellow box. All scale bars, 5 µm. Data are presented as mean values ± 0.5 s.d. Source data are provided as a Source Data file.

interactions between cages and PSH (electrostatic and 6His-Ni²⁺ binding) might be excessively strong, causing them to phase separate together into the same condensates. Small HF and POK cages even without 6His were also predominantly observed inside condensates, and condensate sizes increased from 10 min to 60 min. HF and POK with their rather small sizes might lack enough surface stabilization energies to remain on PSH condensate surfaces. On the other hand, small coalescence-inhibited PSH condensates were stably formed in the presence of large HF oligo and mi3 without 6His (Fig. 1e, yellow box and Supplementary Fig. 2b). Radial profiles of interfacial cages

indicated that HF oligo and mi3 were securely bound on the surface of these small condensates, with the ratios of inner to interfacial distribution remaining mostly unchanged over 24 h (Supplementary Fig. 2c).

These data suggest crucial conditions for the assembly of stable protein condensates. Larger cages were more effective in condensate stabilization, as also suggested by the Pickering emulsion theory. More importantly, interactions between protein cages and condensates must be robust enough to prevent coalescence, but these interactions cannot be overly strong, which causes cage penetration into condensates (Fig. 1f). To further validate this assembly principle, we varied cage-condensate interactions in diverse ways. When the condensate-binding SH3 was additionally fused to HF oligo to enhance binding strength (Supplementary Fig. 1c), cages readily penetrated condensates, resulting in enlarged condensates (Fig. 1g). When 6His tags were removed from HF oligo to reduce binding strength, cage binding to surfaces was evidently decreased, once again resulting in enlarged condensates. We also varied electrostatic interactions between mi3 cages and PSH condensates by altering salt concentration. With added salts and thereby reduced electrostatic interactions, mi3 surface binding was dramatically diminished, leading to condensate growth (Fig. 1h and Supplementary Fig. 2d). At low salt concentrations, with enhanced electrostatic interactions, mi3 cages were found inside condensates and did not function as an interface stabilizer to prevent coalescence.

Assembly of diverse cage-stabilized protein condensates

We found that cage-condensate interactions could be carefully tuned to obtain a delicate balance for preventing coalescence and avoiding excessive cage penetration. Our next step was to assess the applicability of interfacial protein cages to a broader range of protein condensates with varying properties. First, we examined protein condensates resembling those formed by PSH but with increased fluidity. PS-RL48, featuring an extended linker between PRM-SH3 and 6His, undergoes LLPS, forming positively charged (PSH-like) but highly fluidic condensates (Fig. 2a)[30]. Small protein cages readily penetrated fluidic PS-RL48 condensates during LLPS and even into pre-formed condensates (Supplementary Fig. 3a). Large HF oligo and mi3 with 6His, capable of both electrostatic and 6His-Ni^{2+} binding, also penetrated PS-RL48 condensates, while these cages without 6His only weakly bound to condensate surfaces. All these large cages also failed to prevent coalescence (Fig. 2a and Supplementary Fig. 3a). These results indicate that, under comparable interaction conditions, cages are more likely to penetrate fluidic condensates than rigid ones. In the search for optimal cage-condensate interaction, we first reduced the (electrostatic) condensate binding strength of HF oligo with partial 6His tags by mutating HF into a more neutral form[36] (neu-HF oligo) (Supplementary Fig. 3b). Although neu-HF oligo slightly penetrated condensates, condensate coalescence was also slightly reduced (Fig. 2a, yellow box). Therefore, we further weakened the binding strength of neu-HF oligo by gradually lowering Ni^{2+} concentration. Although smaller PS-RL48 condensates were formed with reduced [Ni^{2+}], LLPS was also significantly diminished (Fig. 2b). To compensate for weakened LLPS while maintaining low [Ni^{2+}], the crowding agent PEG[37] was added. While high PEG (4%) caused heterogenous cage aggregations, coalescence-inhibited PS-RL48 condensates were stably formed with 1–2% PEG and low [Ni^{2+}] (Fig. 2b and Supplementary Fig. 3c). The interfacial distribution of cage proteins remained mostly unchanged over 24 h (Supplementary Fig. 3d). This optimization process illustrates how precise interaction adjustment through protein engineering and binding condition tuning enables the discovery of ideal stabilization conditions for target protein condensates.

We next investigated condensates composed of intrinsically disordered proteins (IDPs), which play a vital role as primary scaffold proteins in cellular LLPS[38]. Protein condensates of LAF[39], a well-known LLPS IDP, were similarly formed by mixing 6His-tagged LAF and Ni^{2+}.

The resulting LAF condensates were also highly fluidic (Supplementary Fig. 4a). Unlike PSH and PS-RL48 condensates, however, designed LAF condensates are slightly negatively charged. Consequently, protein cages without 6His were unable to adsorb to condensate surfaces and stabilize them, regardless of the introduction timing (sequential or one-pot) (Fig. 2c and Supplementary Fig. 4b). On the other hand, cages such as HF oligo, mi3, and HF with 6His tags effectively adsorbed on LAF condensate and delayed coalescence. However, condensate sizes still slowly but evidently increased (Supplementary Fig. 4c), indicating that cage-condensate interactions were not strong enough without electrostatic attractions. To further optimize condensate stabilization, 6His-Ni^{2+} interactions were strengthened by gradually increasing [Ni^{2+}]. Stable and coalescence-blocked LAF condensates were formed at higher [Ni^{2+}] (100 μM), although excess metal ions (200 μM) caused droplet aggregation (Fig. 2d and Supplementary Fig. 4d). Observed stabilization was specific for 6His-Ni^{2+} interactions since condensate binding of mi3 without 6His was not influenced by [Ni^{2+}] increases (Supplementary Fig. 4d). Although the cage signals inside condensates slightly increased, the size and structure of caged LAF condensates remained mostly unchanged over 24 h (Supplementary Fig. 4e, f). This result also highlights the importance of utilizing two orthogonal binding mechanisms to fine-tune cage-condensate interactions.

Lastly, we explored condensates formed through non-Ni^{2+} mediated LLPS. The phase separable PRM-SH3 motif was tandemly repeated (PRM-SH3-PRM-SH3-6His, PS2H) to enhance the LLPS propensity of the scaffold. PS2H underwent LLPS at a low salt concentration ([NaCl] = 60 mM), without requiring any protein clustering, into highly fluidic and positively charged condensates (Supplementary Fig. 5a), similar to PS-RL48 condensates. However, unlike PS-RL48 condensates, PS2H condensates were effectively stabilized by large HF oligo and mi3 cages without the need for any cage-condensate binding adjustment (Fig. 2e and Supplementary Fig. 5b). Small and coalescence-blocked PS2H condensates were formed with HF oligo and mi3, regardless of 6His, due to the absence of Ni^{2+}. Enhanced electrostatic interactions between cages and condensates under the lowered salt concentration likely contribute to this effective stabilization. However, a further increase in cage-condensate interactions by SH3 fusion or [NaCl] decreases (40 mM) caused cage penetration and condensate coalescence (Fig. 2f and Supplementary Fig. 5b). In addition, small cages still readily penetrated condensates (Supplementary Fig. 5b), once again highlighting the importance of interfacial cage sizes. PS2H condensates covered with large cages were stable over 24 h (Supplementary Fig. 5c). Electrostatic binding between large cages and condensates might be sufficient for surface stabilization in certain types of condensates.

In summary, our systematic exploration of various protein condensates under diverse LLPS conditions demonstrates the versatility and adaptability of interfacial protein cages to stabilize protein condensates.

Size-controlled assembly of cage-stabilized protein condensates

We envisioned that the formation of cage-stabilized protein condensates starts with rapid nucleation and growth, possibly accompanied by early coalescence. Subsequently, protein cages, possessing proper condensate binding strength and sizes, begin to adsorb onto condensate surfaces. The growth of condensates through coalescence halts as the condensates become sufficiently covered by cages. In this scenario, we believed that condensate sizes can be determined by relative quantities of condensates and cages for a given condensate/cage pair (Fig. 3a). At low [cage], the total surface area of early small condensates (before extensive coalescence) is too large to be effectively protected by cages. Consequently, these partially protected condensates continue to fuse into larger ones until the total surface area diminishes enough to be sufficiently covered by cages. On the other hand, at high [cage], even small condensates with a large total surface area can be effectively stabilized by cages.
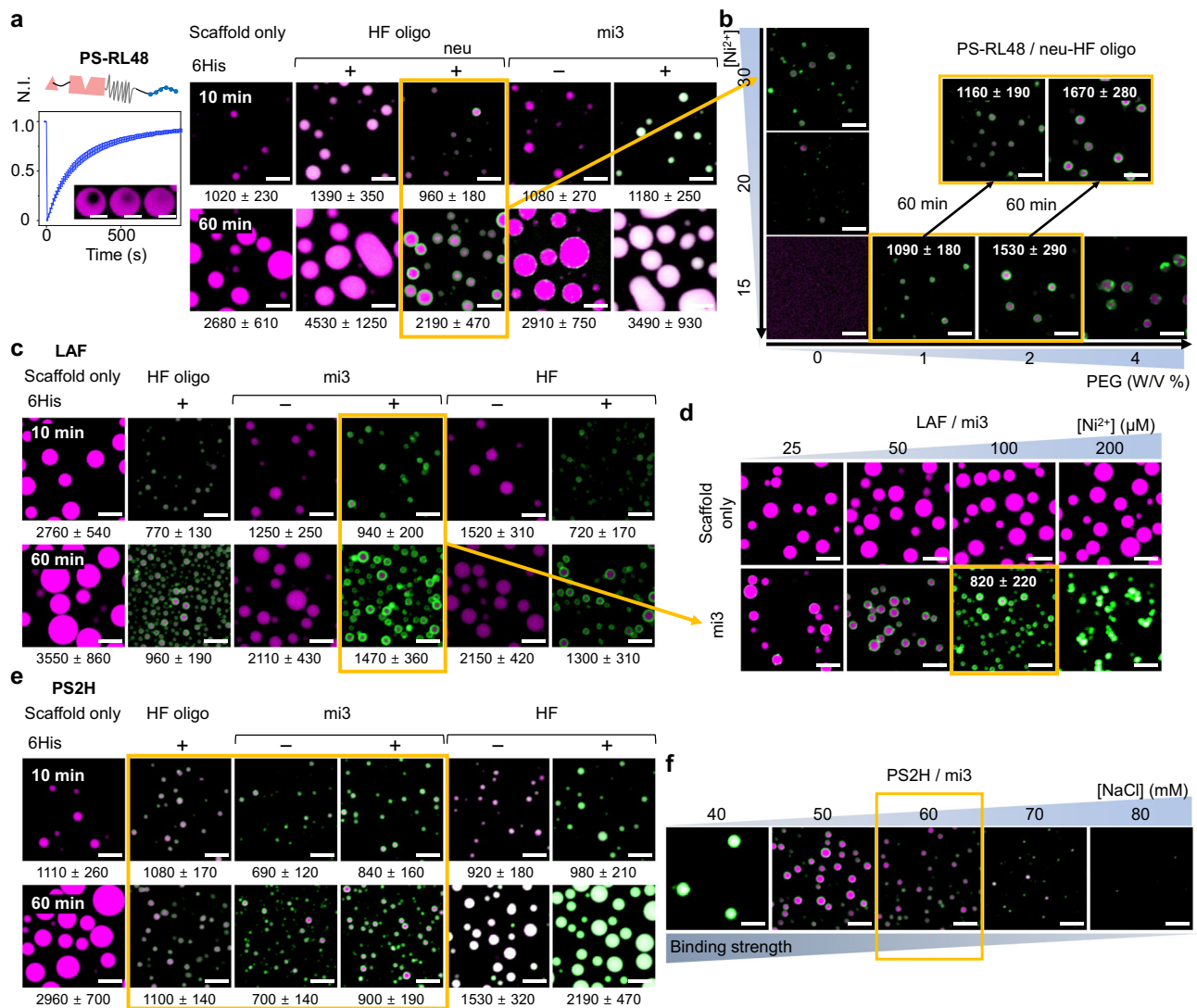
Fig. 2 | Surface stabilization for diverse fluidic protein condensates. a Confocal images of fluidic PS-RL48 condensates (FRAP data shown left, magenta, $n = 10$ condensates), phase separated in the presence of indicated protein cage variants (green) (one-pot assembly), after 10- and 60-min incubation with average diameters. Images for PS-RL48 condensates with neu-HF oligo that has undergone additional optimization (a yellow arrow) are marked with a yellow box. **b** Confocal images of neu-HF oligo-treated PS-RL48 condensates with systematically varied interaction strengths between neu-HF oligo and PS-RL48. [Ni²⁺] was decreased to reduce interaction strength, and PEG was added to stimulate LLPS. Effectively stabilized (coalescence-inhibited for 60 min) condensates were indicated with yellow boxes with average diameters. **c** Confocal images of cage-treated (one-pot)

LAF condensates with average diameters. Cage-condensate assemblies that have undergone additional optimization (a yellow arrow) are marked with a yellow box. **d** Confocal images of LAF condensates without (scaffold only) or with interfacial mi3 at increased [Ni²⁺]. Effectively stabilized condensates were indicated with a yellow box with an average diameter. **e** Confocal images of cage-treated (one-pot) PS2H condensates with average diameters. Surface-stabilized (coalescence-inhibited) protein condensate images are indicated with a yellow box. **f** Confocal images of mi3-treated PS2H condensates at different salt concentrations. All scale bars, 5 µm. Data are presented as mean values ± 0.5 s.d. Source data are provided as a Source Data file.

To control the size of PSH condensates with interfacial HF oligo, the PSH/HF oligo ratio was extensively varied. The size diagram of confocal microscope images shows HF oligo-PSH condensates with sizes ranging from nano- to micro-scale (Fig. 3b). At a fixed [PSH], the condensate size decreased as [HF oligo] increased, and at a fixed [HF oligo], the condensate size increased as [PSH] increased. PSH condensates as large as 2 µm were assembled with 50 µM PSH (Supplementary Fig. 6a). Due to the optical resolution limit, the sizes of small condensates were analyzed using negative-stained TEM (Fig. 3c). With varying [HF oligo] (from 10 nM to 40 nM) at a fixed [PSH] (20 µM), the assembled condensate sizes ranged from ~150 nm to 860 nm on average with high homogeneity (Fig. 3d). Further increases in [HF oligo] caused heterogeneous aggregation of condensates and excess cages, suggesting that ~100 nm might be the size limit of HF oligo-

stabilized PSH condensates (Supplementary Fig. 6b–d and Supplementary Note 1).

Condensate formation yield was assessed by separating condensates from the surrounding solution through centrifugation. Most PSH and HF oligo were included in condensates, offering an excellent formation yield (Fig. 3e). Moreover, when [HF oligo] increased at a fixed [PSH], the PSH quantity in cage-stabilized condensates remained constant while surface-bound HF oligo increased. These data support our cage-stabilization mechanism, where small condensates, with a large total surface area, are covered by more cages (Fig. 3a). This also indicates that condensate coalescence and subsequent size control by cages do not influence LLPS propensity. By altering [condensate]/[cage] ratios, we were also able to extensively vary the sizes of all assembled condensates such as PSH/mi3,
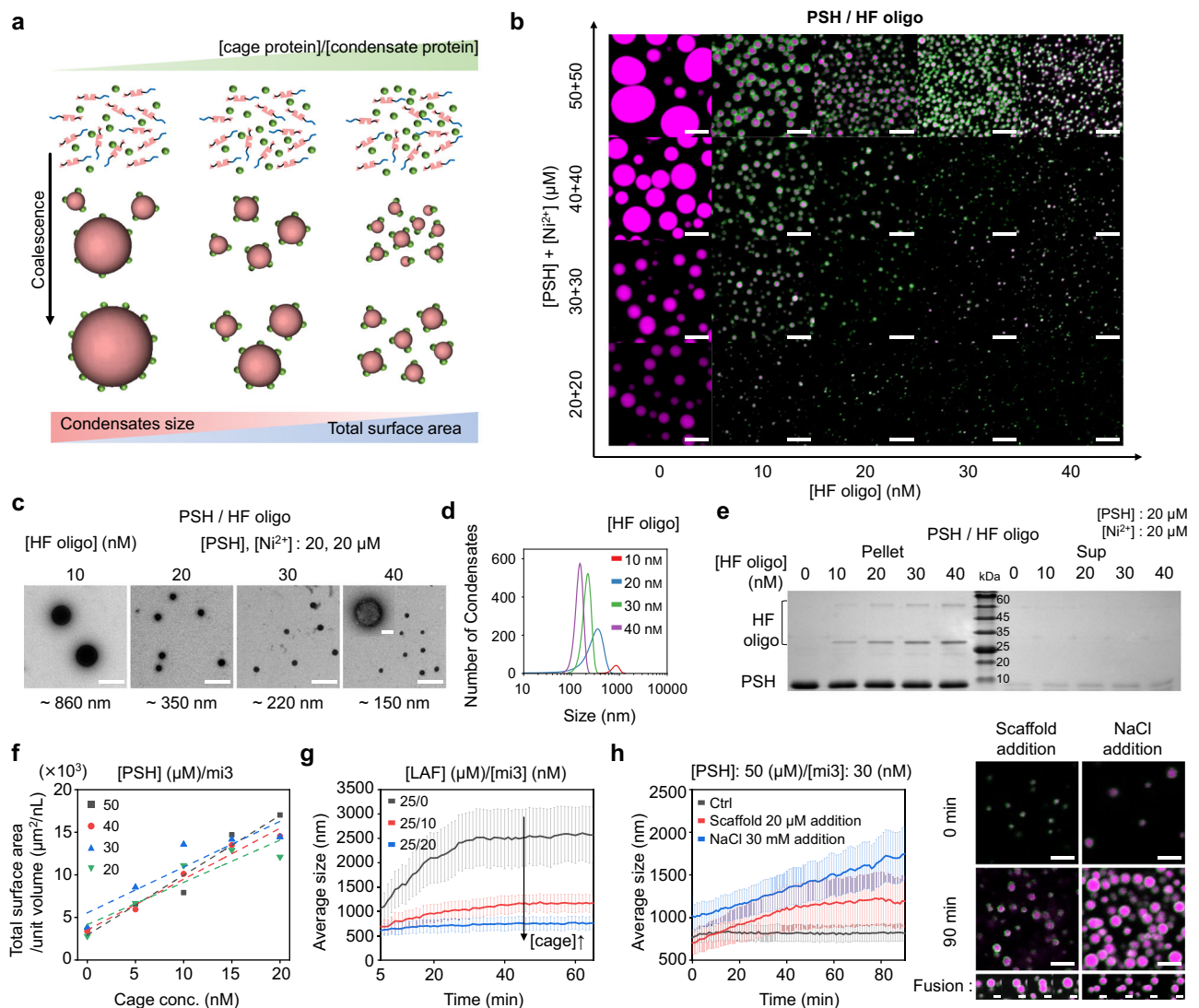
Fig. 3 | Size-controlled assembly of cage-stabilized protein condensates.
a Schematic illustration of condensate size variation by [interfacial protein cages]/[condensate] ratios. **b** The size diagram of HF oligo-stabilized PSH condensates with varying [PSH]/[Ni^{2+}] and [HF oligo]. Confocal images were taken after 1 h incubation upon LLPS. **c** Negative-stained TEM images of nano-sized HF oligo-PSH condensates. Average condensate sizes are indicated below. **d** Size distribution profiles (based on negative-stained TEM images as shown in Fig. 2c) of nano-sized HF oligo-PSH condensates. **e** A denatured gel image of centrifuged condensates (Pellet, left) and remaining substances in the dilute phase (Sup, right) assembled with fixed [PSH] and increasing [HF oligo]. **f** Plots for estimated total surface areas

of PSH condensates at varying concentrations (20–50 μM) as a function of cage concentrations. Each dot represents the outcome for each condition, with a linear estimate line fitted to the data. **g** Growth curves of mi3-LAF condensates over time with varying mi3 cage concentrations ($n > 35$ condensates). **h** Growth curves of PSH/mi3 condensates over time with extra PSH scaffold or NaCl addition ($n > 100$ condensates). Confocal images before and after addition are presented on the right. The fusion process for each case is shown below. Data are presented as mean values ± 0.5 s.d. Source data are provided as a Source Data file. Scale bars, **b**, **g**, **h**, 5 μm. **c**, **h** (bottom) 1 μm (100 nm for the enlarged image in (**c**)).

PS-RL48/HF oligo, and LAF/mi3 condensates with high yields (Supplementary Fig. 7).

Total condensate surface areas were estimated based on the average sizes and internal scaffold protein densities[30] of the condensate (Supplementary Fig. 8a and Supplementary Note 2), with the assumption that most scaffold and cage proteins participated in assembly (Fig. 3e and Supplementary Fig. 7c). For PSH condensates formed with varying PSH concentrations (Supplementary Fig. 7a), the total surface area exhibited a linear correlation with interfacial [mi3 cage] (Fig. 3f), supporting our model for size control (Fig. 3a). Additionally, at a given [cage], total surface area values were fairly similar across all examined scaffold concentrations (20–50 μM), further supporting that [interfacial cage] dictates the stabilizable total surface area. Fusion between partially cage-covered condensates occurred more slowly than between naked condensates, likely due to the

reduced interfacial tension caused by the cages (Supplementary Fig. 8b, c), consistent with a previous report on Pickering biomolecular condensates[26]. Time-lapse growth analysis showed that, compared to condensates without cages, those with cages showed a reduced growth rate, even at identical scaffold concentrations, with more cages leading to slower growth (Fig. 3g). Condensate growth was also immediately inhibited when cages were sequentially added to pre-formed condensates (Supplementary Fig. 8d). When extra scaffold proteins were introduced to cage-stabilized condensates, the size of the condensates readily increased, and coalescence was also observed, suggesting that the size increase due to scaffold recruitment reduced surface cage coverage, promoting condensate coalescence (Fig. 3h and Supplementary Fig. 8e). A rapid increase in condensate size via coalescence was also induced by weakening the strength of cage-condensate interactions through salt addition (Fig. 3h).

Many factors such as stabilization energy, the kinetics of LLPS and condensate-cage binding, and condensate densities, likely influence condensate sizes. Nonetheless, size control through [condensate]/[cage] variations was highly consistent and reliable, without requiring time-dependent kinetic manipulation. Moreover, the search for conditions to reach target sizes was straightforward, with predictable size changes.

The structure of cage-stabilized protein condensates

We next investigated the structural intricacies of fabricated protein condensates, placing particular emphasis on the distribution of interfacial cages around the condensates. The classical Pickering-type emulsification theory predicts the localization of Pickering agents to form a monolayer at the phase boundary[25]. The core-shell structures of micro-sized protein condensates were visualized using confocal microscopy imaging and subsequent Z-stacking (Fig. 4a). However, the inherent resolution limit of light microscopy prevented confirmation of shell formation by cages on smaller condensates, and precise cage locations at the condensate interfaces remained unknown. To address this limitation, we employed transmission electron microscopy (TEM)-based methods, enabling the visualization of individual protein cages. Negative-stained TEM images of various protein condensates clearly indicated that protein cages were densely located on condensates (Fig. 4b and Supplementary Fig. 9a). Nevertheless, these projection TEM images, with heavy metal staining, still do not provide information on the relative positions of protein cages on condensate surfaces.

We next employed cryo-EM, which has the potential to distinguish different electron density patterns of protein condensates and cages without heavy metal staining and sample drying. For cryo-EM analysis, protein condensates must be trapped in an ice layer, which needs to be thinner than 100-200 nm for effective electron transmission across the sample[40]. While typical protein condensates grow rapidly to micro-size, our stabilized condensates can be controlled in size down to ~100 nm. Small mi3-stabilized condensates were prepared and successfully trapped in thin ice layers for cryo-EM analysis. Representatively, rigid PSH condensates and disordered LAF condensates with mi3 were examined. Surface-bound mi3 cages and protein condensates with high electron densities were clearly visualized for both PSH and LAF condensates (Fig. 4c and Supplementary Fig. 9b, c). Interfacial mi3 cages were fairly uniformly located on the condensate surface, suggesting mi3 monolayer structures on the condensates.

We further extended cryo-EM to electron tomography (ET) to fully reconstruct 3D structures of cage-stabilized condensates. A series of tilting cryo-EM images were aligned and used to reconstruct tomograms (Fig. 4d, Supplementary Fig. 10 and Supplementary Video 2). These tomograms were then segmented to create a 3D volume model, with GFP-fused mi3 represented as a 25 nm-sized sphere since flexibly fused GFP was not clearly visualized in cryo-EM images (Supplementary Fig. 10a). The 3D volume model clearly revealed a highly packed monolayer shell of mi3 on a LAF condensate (Fig. 4e and Supplementary Video 3). However, cage densities appeared obscure in certain areas of the condensate surface due to the presence of 10 nm gold nanoparticles used as fiducial markers. These nanoparticles closely aligned with regions where cages were undetectable (Supplementary Fig. 10c), potentially blocking cage binding on the condensate surface and, due to their high electron density, limiting cage visibility in nearby regions. These structural data strongly support our assembly principles of cage-stabilized protein condensates. PSH condensates were also uniformly covered with a mi3 monolayer (Supplementary Fig. 11a). In cryo-ET structures, many condensates were noticeably squeezed into ellipsoidal shapes with ~150 nm thicknesses. We suspect that the surface tension at the air-water interface[41] exerted upon condensate embedment in a thin water layer might have caused the squeezing of liquidic protein condensates that are larger than the water layer. In fact, small condensates (~100 nm) mostly retained their spherical shapes (Fig. 4e).

Internal cage entities might not be visible on the tomogram due to the high internal density of the condensate. To further confirm the absence of cages inside condensates, tomograms were obtained with intentionally inserted protein cages. A small amount of HF-6His was added during the assembly of mi3-PSH condensates. We anticipated that HF-6His would be located inside the mi3-coated PSH condensates, as HF-6His cages readily penetrate PSH condensates (Fig. 1e). Smaller HF cages were clearly observed in tomograms, while all mi3 cages were on the condensate boundary (Fig. 4f). Close examination of tomograms suggested that interfacial mi3 cages maintained a relatively consistent contact angle with condensate interfaces (Fig. 4g and Supplementary Fig. 11b). The cages were only slightly buried in the condensates, and the contact angles remained largely unchanged by increases in the interaction strength between cages and condensates (Supplementary Fig. 11c). Pickering agents having a contact angle lower than 90° on a highly curved interface is a commonly known feature in Pickering emulsion[22]. However, we cannot rule out the possibility that condensates have protein brush-like surfaces[42], which are difficult to visualize due to low and sporadic electron densities. Surface protein brushes will further influence cage interactions on condensate surfaces, making it challenging to precisely define contact angles. Additionally, the flexible GFP fusions on mi3 complicate the accurate analysis of minor changes in contact angles. Nonetheless, the contact angles were slightly smaller on rigid and denser PSH condensates than on LAF condensates (Fig. 4g and Supplementary Fig. 11b). It is also noteworthy that mi3 coverage on PSH condensates was clearly less complete than on LAF condensates (Fig. 4h). It is possible that complete interface covering might not be required to block coalescence for certain condensates and LLPS conditions. The surface mi3 density on stabilized PSH condensates, calculated from cryo-ET structures, was ~750 cages/μm² (Supplementary Fig. 11 and Supplementary Note 3). This value is comparable to those estimated from confocal images (Supplementary Fig. 8a), despite differences in experimental conditions and estimation methods. A previous study on Pickering nanotube-emulsified oil-in-water droplets demonstrated that the extent of droplet coverage by Pickering agents varied with the concentration of added nanotubes[43]. Similarly, in Pickering-stabilized biomolecular condensates within cells, the condensates were not completely covered by interfacial protein clusters[26].

Dynamic behaviors of cage-stabilized protein condensates

Finally, we examined whether surface-covered protein condensates retain dynamic properties, such as the ability to selectively exchange materials with the outside. Identical condensates were separately prepared with different dye labels (Cy5 and Cy3) for all examined condensates (PSH, PS-RL48, LAF, PS2H) and mixed. For fluidic condensates (PS-RL48, LAF, PS2H), the two dyes were homogeneously distributed in all condensates (Fig. 5a and Supplementary Fig. 12a, b), indicating dynamic scaffold protein exchanges between condensates without coalescence. On the other hand, scaffold exchange was not observed for rigid PSH condensates (Fig. 5a and Supplementary Fig. 12c). Protein exchange between fluidic condensates was gradual but fairly rapid, reaching new equilibrium states before 10 min after mixing, while the composition of PSH condensates remained mostly unchanged even after 60 min incubation (Supplementary Fig. 12a–c). In the absence of cages, only PSH condensates did not exchange their scaffold proteins (Supplementary Fig. 12d), indicating that condensate characteristics were well preserved even after dense wrapping with interfacial cages. The presence of cages did not affect the fluidity of cage-stabilized condensates (Supplementary Fig. 12e).

We next investigated the selective recruitment of outside materials, one of the features of condensate materials. Negatively charged DNA (300 bp) was well recruited into positively charged PSH and PS-RL48 condensates but not into negatively charged LAF condensates (Fig. 5b). 6His-tagged mCherry was well recruited into all Ni²⁺-
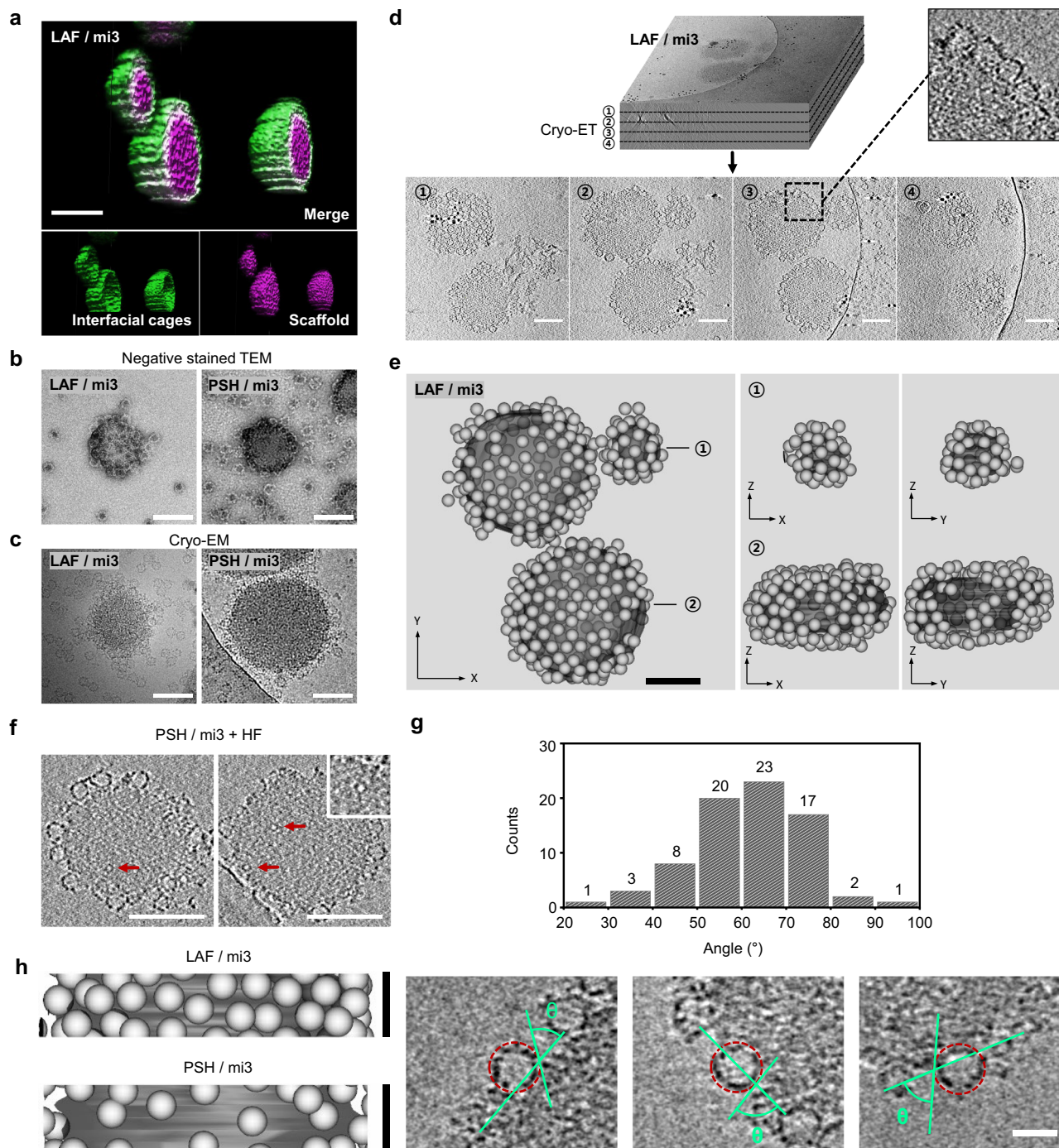
Fig. 4 | Structures of surface-stabilized protein condensates with interfacial protein cages. a Confocal Z-stack 3D representation of mi3-LAF condensates (LAF: magenta, mi3: green). **b** Negative-stained TEM images of mi3-LAF (left) and mi3-PSH (right) condensates. **c** Cryo-EM images of mi3-LAF (left) and mi3-PSH (right) condensates. **d** Reconstructed tomograms of mi3-LAF condensates. Four images of equal Z-distances (~40 nm) are shown below to demonstrate cage distributions at the bottom/middle/top of the condensate. Thick black dots are 10 nm gold nanoparticles used as a fiducial marker. **e** 3D volume models of mi3-LAF condensates (left: top view of the whole tomogram, right: front and side view of selected condensates). mi3 cages are shown as gray spheres. **f** Tomogram slices of mi3-PSH condensate with ferritin cages (red arrows) located inside the condensate. **g** Contact angles of mi3 cages on LAF condensates with a representative tomogram slice image. Exemplary cages and contact condensate surfaces are indicated with red dotted circles and lines, respectively. **h** Side views of 3D volume models of mi3-stabilized LAF (top) and PSH (bottom) condensates. Scale bars, **a** 5 μm. **b, c, d, e, f** 100 nm. **g** 25 nm. **h** 50 nm. Source data are provided as a Source Data file.

coordinated condensates except rigid PSH condensates. These biomolecules could also be strongly encapsulated in condensates by simply adding them during cage-stabilized condensate assembly (Supplementary Fig. 13a). For more controlled, interaction-driven recruitment, antibody-binding protein G was introduced to PSH condensates[44]. Antibodies were effectively encapsulated in cage-

stabilized condensates only with fused protein G (Fig. 5c and Supplementary Fig. 13b). The dynamic and reversible nature of condensates is clearly distinct from similarly dense but irreversible protein aggregates. While condensate sizes increased by extra scaffold proteins (Supplementary Fig. 8e), the sizes remained unaltered by protein cage addition since the condensates were already fully stabilized
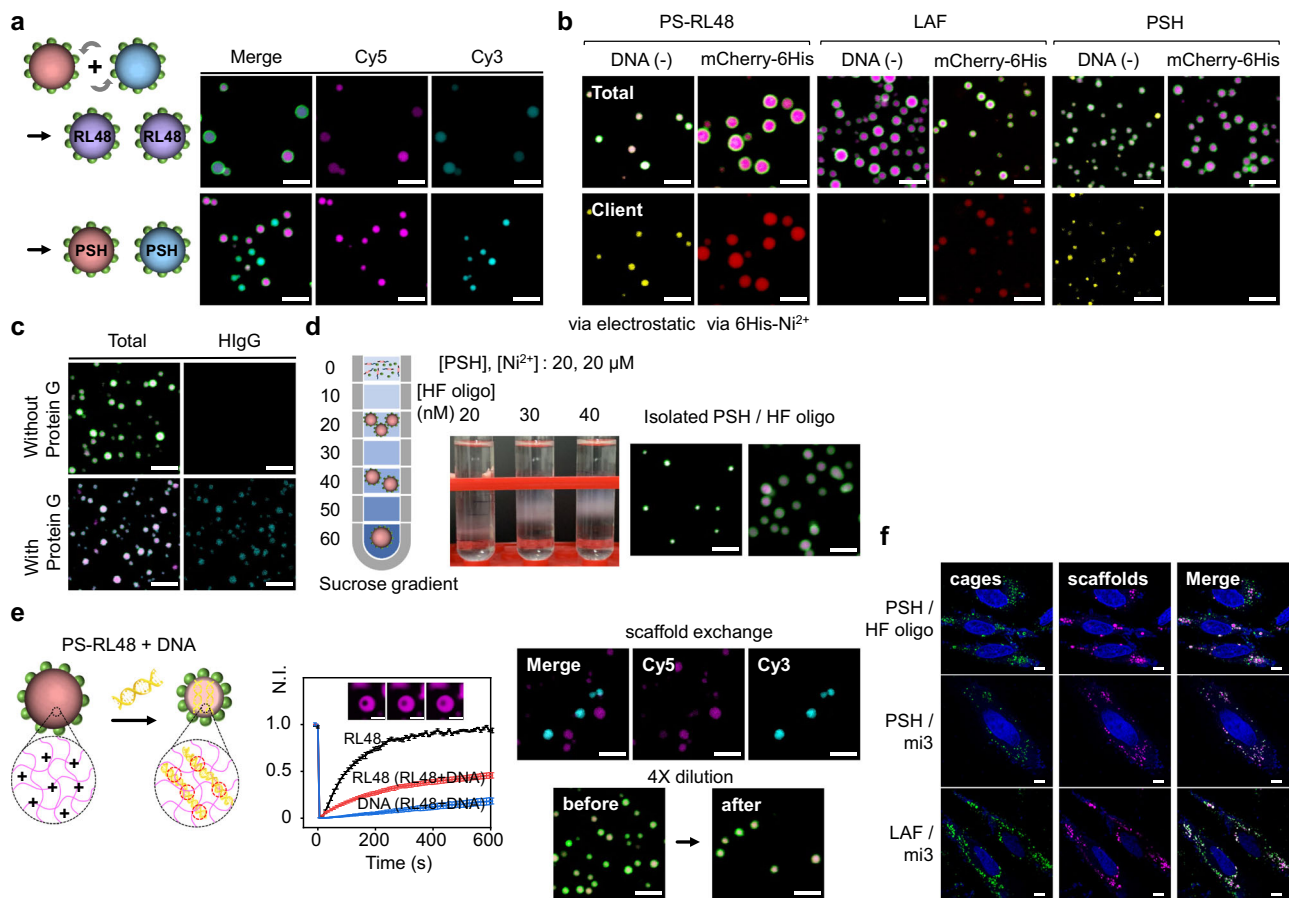
Fig. 5 | Dynamic behaviors of cage-stabilized protein condensates. a Confocal images of separately labeled (Cy5 magenta, Cy3 cyan) cage-stabilized condensate mixtures after 10 min incubation upon mixing (top: PS-RL48 condensates, bottom: PSH condensates). **b** Confocal images of cage-stabilized condensates with externally added client biomolecules (DNA (yellow) and mCherry-6His (red)). **c** Confocal images of HF oligo-PSH condensates (with or without protein G fusion to PSH) assembled with antibody (cyan). **d** Sucrose gradient centrifugation of cage-stabilized PSH condensates. A picture of sucrose gradient centrifuged HF oligo-PSH condensates with different sizes with schematics and exemplary confocal images of isolated PSH condensates in sucrose solution are shown. **e** Fluidity change of cage-stabilized condensates. DNA recruited into fluidic PS-RL48 condensates induces additional PS-RL48 clustering around DNA, resulting in decreased size and fluidity of condensates (left: schematics). FRAP recovery profiles (red: PS-RL48, blue: recruited DNA, $n = 10$ condensates) and confocal images (PS-RL48) of the bleached DNA-containing PS-RL48 condensates are shown in the middle. A FRAP profile for fluidic PS-RL48 condensates is shown as a control (black). Confocal images for separately labeled, DNA-recruited PS-RL48 condensate mixtures after 60 min incubation (right top) and 4X diluted condensates (right bottom) are shown in the right. Data are presented as mean values ± 0.5 s.d. **f** Confocal images of HeLa cells treated with HF oligo-PSH, mi3-PSH, and mi3-LAF condensates. Scaffold (magenta), cage (green), and DAPI (blue). Scale bars, **a**–**e** 5 μm. **f** 10 μm. Source data are provided as a Source Data file.

(Supplementary Fig. 13c). To examine the effects of interfacial cages on client recruitment, we compared the DNA recruitment of PSH condensates with and without cages (Supplementary Fig. 13d, e). No size selectivity was observed across different DNA lengths (300 bp, 500 bp, 1000 bp), and recruitment speed remained unaffected over time (1 min, 2 min, 5 min), though larger molecules or faster time points may still be influenced by the cages.

Condensates can also be disassembled by changing the solution conditions to discourage LLPS. For instance, concentration dilution gradually dissolved fluidic PS-RL48 condensates with interfacial cages (Supplementary Fig. 14a). Interestingly, rigid PSH condensates exhibited unexpectedly high resistance against various external perturbations. The cage-coated structures remained intact after dilution (or even full buffer exchange by dialysis) and at various temperatures (Supplementary Fig. 14b). Therefore, cage-stabilized PSH condensates could be isolated from the assembly solution (Fig. 5d) and also further separated based on their sizes using sucrose gradient centrifugation (Supplementary Fig. 14c). Cage-stabilized PSH condensates could still be disassembled when key interactions were disturbed, such as by metal chelators to reverse 6His-Ni^{2+} coordination[30]. These data indicate that the resistance of cage-stabilized condensates against external

changes is mainly governed by the dynamicity of core condensates. Therefore, the stability of our assembled condensates might be controllable by manipulating condensation forces. In fact, when DNA (300 bp) was recruited into fluidic PS-RL48 condensates, the condensate size was notably reduced (Supplementary Fig. 14d). Many PS-RL48 proteins could assemble around DNA, which might lead to enhanced condensation and a size decrease. Cage-stabilized PS-RL48 condensates became significantly less fluidic upon DNA recruitment, and protein exchange between condensates was also vastly slowed (Fig. 5e and Supplementary Fig. 14e). These DNA-inserted condensates were highly resistant to concentration dilution. Scaffold clustering enhancement can be a selective, reversible, and physiological strategy to increase the stability of cage-stabilized condensates.

Lastly, we examined the interaction of caged protein condensates with cells and found that both caged and uncaged condensates were able to penetrate into cells. While the precise mechanism of condensate penetration remains unclear and will require further study, several reports in the literature have documented cellular uptake of biomolecular condensates[11,12,45]. Three distinct caged condensates (PSH/HF oligo, PSH/mi3, and LAF/mi3) readily penetrated live cells and localized within the cytosol (Fig. 5f and Supplementary Fig. 15a).

The spherical structure of the condensates was maintained post-penetration, although the organization of interfacial cages around them became heterogeneous (Supplementary Fig. 15b). Some condensates showed internal cage signals, while others exhibited a reduction or complete absence of cages. Time-lapse imaging also revealed the dynamic redistribution of interfacial cages around the condensates in the cytosol (Supplementary Fig. 15c). Additionally, occasional fusion events between cell-penetrated condensates were observed, consistent with the liquid-like behavior of protein condensates (Supplementary Fig. 15d). Cell-penetrated condensates remained stable in live cells, retaining their condensed droplet structures even after 1 day (Supplementary Fig. 15e). On the other hand, all condensates became highly fluidic in cells, and the fluidity increased over time (Supplementary Fig. 15f and Supplementary Note 4). Caged condensates did not induce noticeable morphological changes or toxicity in cells (Supplementary Fig. 15g).

Discussion

In this study, we present a reliable approach for assembling stable protein condensates with sustained integral structures, additional boundary functions, and well-defined sizes ranging from micro- to nanoscale dimensions. Routes to find optimal interfacial protein cages and LLPS conditions for given condensates are straightforward, primarily adjusting interactions between cages and condensate-forming proteins. Precise and systematic adjustment was possible with fully protein-based interactions. We envision that other biopolymers with defined binding moieties and sizes could also be developed as interfacial stabilizers. The assembly is both simple and efficient as a one-pot assembly with high overall yields. Size control, achieved by altering [condensate]/[cage] ratios, is also undemanding. We believe that our method is accessible to many researchers, opening avenues for diverse exploration and applications of protein condensates as biomaterials.

As a practical approach to designing Pickering cages for specific protein condensates, we suggest starting with the selection of relatively large, surface-modifiable protein cages, such as ferritin or mi3. The next step is to choose appropriate cage-condensate interactions, with electrostatic forces being a particularly effective option for stabilizing condensates. Both attractive and repulsive interactions can be employed, and their strength can be modulated by adjusting salt concentrations. Thus, careful assessment of condensate charges and engineering of cage surfaces would be critical. Additional interactions, such as metal coordination or specific peptide binding, are likely necessary to fine-tune stabilization. Once cages and interactions are selected, initial assessments should be conducted on both pre-formed and co-formed condensates under varied binding conditions. Cage-condensate interactions can then be further tuned to achieve the desired stabilization (Supplementary Fig. 16).

We fabricated cage-stabilized protein condensates as small as 100–150 nm with interfacial cages of ~30 nm. Determining factors for this size limit (e.g., cage size, LLPS speed, and condensate liquidity) are not yet clear, requiring further investigation. Nevertheless, our ability to stably isolate these small condensates enabled the 3D structure visualization of protein condensates with interfacial entities using cryo-ET. Interfacial cages are only slightly buried in condensates with contact angles between 40 and 80 degrees, and PSH condensates could be stabilized even without full cage coating. We believe that our strategy can be used to reveal unknown structural information on diverse biomolecular condensate-related activities. For example, we plan to investigate changes in interfacial and internal structures by monitoring stabilized protein condensates subjected to external stimuli. It will also be interesting to encapsulate specific biomolecules inside cage-stabilized condensates and visualize their structures under condensate environments using cryo-ET.

Our work on condensate surface stabilization will also significantly contribute to understanding mechanisms that modulate cellular MLO sizes. P granules in Caenorhabditis elegans were similarly stabilized by protein clusters[26], and stress granule sizes were also influenced by surface-bound protein-RNA clusters[46]. Surface accumulated RNAs could also stabilize protein condensates[47,48]. We demonstrated that this stabilization mechanism is not a rare phenomenon limited to certain condensates but rather universally applicable and tunable. Our cryo-ET data provide clear structural evidence for this Pickering-type emulsification of protein condensates. Future work will focus on elucidating the mechanism of action of interfacial entities on protein condensates in greater detail. For instance, we observed that the interfacial cage density on stabilized condensates increased with higher concentrations of added cages (Supplementary Fig. 8a). In Pickering emulsions, the interfacial tension of droplets similarly decreases as more Pickering agents accumulate at the interface[49]. Further investigation into the physics of interfacial cage stabilization on protein condensates will provide deeper insights into the biophysical principles governing Pickering biomolecular condensates. In addition, with fully protein-based interfacial entities, our strategy could be further developed to manipulate MLOs in cells.

While this study establishes a foundation for the development of dynamic and functional condensate materials, tailoring methods need further refinement for diverse applications in biotechnology and medicine. For example, it will be necessary to develop strategies to encapsulate non-phase separable cargos, such as biopharmaceuticals, in high quantities, and to design interfacial cages suitable for these cargo-heavy condensates. Additionally, it is crucial to develop methods for further stabilizing condensate assembly structures, as cage-covered condensates can be disassembled when LLPS driving forces or equilibrium states are disrupted. Additional clustering of condensate-forming proteins can be a potent approach, as demonstrated by the fact that fluidic PS-RL48 condensates became more resistant to equilibrium shift by DNA recruitment and subsequent PS-RL48 clustering around DNA. We found that size-controlled protein condensates can penetrate live cells while maintaining the structure and fluidity of condensate droplets within the cytosol. While this discovery suggests potential future applications, such as using these condensates for cellular delivery or as extracellularly formed artificial organelles, the underlying mechanisms of condensate penetration remain largely unknown. Extensive future research will be essential to better understand this process and to explore ways to manipulate these condensates within cells for potential therapeutic applications.

Methods
Preparation of engineered proteins
All genes encoding indicated proteins were cloned into the pET-21a(+) plasmid (Novagen). Cloned plasmids were transformed into BL21(DE3), and the cells were grown in LB until A600 reached 0.6–0.8. 1 mM IPTG (LPS solution) was added, and the cells were incubated overnight at 20 °C. Protein-expressing cells were harvested by centrifugation and sonicated. The cell lysates were centrifuged at $15,922 \times g$ for 15 min. 6His-tagged scaffold proteins and GFP-6His were purified by using Ni-IDA resins (BioProgen). To remove residual nickel ions in purified proteins, 500 μM EDTA was added to the purified protein eluents, and overnight dialysis was performed twice in $1 \times$ PBS (KH_2PO_4 1.1 mM, NaH_2PO_4 3 mM, NaCl 160 mM). For HF and mi3 variants, supernatants were heated at 60 °C for 10 min before being purified using size exclusion chromatography (SEC) with a Sepacryl S-300 column (buffer: Tris 50 mM, NaCl 150 mM, pH 7.2). POK variants were also purified by SEC, but without heat treatment. Protein cages were then dialyzed in $1 \times$ PBS. HF oligos were prepared by mixing Z_E fused HF and Z_R fused HF at a 1: 10 ratio for 3 h (Supplementary Fig. 1c)[35]. The mixtures were purified using Ni-IDA resins. 500 μM EDTA was added to the purified protein solution to remove free nickel ions, and the solution was dialyzed twice in 1×PBS.

Fluorescent dye labeling of proteins

Proteins were tagged using cyanine 3 (Cy3) or cyanine 5 (Cy5) N-hydroxysuccinimide (NHS) ester (Lumiprobe), dissolved in dimethyl sulfoxide (DMSO). The labeling procedure was performed in 1 × PBS. Protein samples were conjugated with cyanine NHS ester at a 1:1 protein-to-dye ratio to minimize multiple dye molecules labeling a single protein. After incubating for 2 h at 25 °C with gentle mixing, dye-conjugated proteins were purified using PD-10 desalting columns (Sephadex™ G-25 M, GE Healthcare) to remove unreacted dyes. Dye-labeled proteins were mixed with unlabeled proteins in a 1:9 ratio before use.

Protein phase separation and confocal microscopy imaging

6His tagged scaffold proteins were filtered (0.2 μm DISMIC-25CS, Advantec) and stored in 1×PBS before LLPS. Protein condensates were formed by adding $NiCl_2$ to scaffold proteins under indicated buffer conditions. PS2H condensates were generated by mixing scaffold solution (in 1× PBS) and NaCl-free phosphate buffer (KH_2PO_4 1.1 mM, NaH_2PO_4 3 mM) to meet the specified scaffold and NaCl concentrations. After 2 min incubation, samples were transferred to 10% BSA-passivated μ-slide 18 well (ibidi). For long-term observation, the passivation method was adjusted by increasing BSA concentration (up to 30%) or using Tween 20 as a coating material. To prevent evaporation, empty wells were filled with buffer, and the cover and slide were tightly sealed. Condensates were analyzed by the A1R HD25 confocal microscope (Nikon) using a 60×/1.40 Apochromat Lambda D Oil objective lens. Fluorescent images were taken at 488 nm for GFP-fused protein cages, 561 nm for Cy3-tagged proteins, and 647 nm for Cy5-tagged proteins. The images were processed and analyzed using the NIS Elements software (Nikon). Confocal Z-stack 3D images were obtained in an agarose gel to prevent condensate motions.

Fluorescence Recovery After Photobleaching assay (FRAP)

For in vitro FRAP analysis, photobleaching was performed on circular regions of ~5 μm protein droplets, with regions of bleaching (ROB) areas accounting for less than 10% of the total droplet area. Cy3- or Cy5-tagged protein droplets were bleached using a 561 nm or 647 nm laser, respectively. Time-lapse images were captured over a 15 min period. The intensities of ROB, background (BG), and reference (REF) regions were measured using NIS Elements. Recovery curves were plotted $(I_{ROB} − I_{BG})/(I_{REF} − I_{BG})$ (I_X: Intensity of X region.) against time. $(I_{ROB} − I_{BG})/(I_{REF} − I_{BG})$ before photobleaching was set to 1 and $(I_{ROB} − I_{BG})/(I_{REF} − I_{BG})$ right after photobleaching was set to 0[30]. The normalized fluorescence intensity (nFI) was fitted to a simple exponential model, $nFI(t) = b(1 − e^{−at})$, using Origin. For in-cell FRAP analysis, 1–2 μm condensates were randomly selected regardless of cage distribution. To capture rapid fluorescence recovery, the imaging interval was shortened, and image resolution was reduced. Due to rapid recovery, fluorescence could begin restoring before the initial post-bleach image was captured, with a minimum delay of 1.2 s (including photobleaching and image acquisition). $(I_{ROB} − I_{BG})/(I_{REF} − I_{BG})$ before photobleaching was set to 1 and subsequent values were adjusted proportionally without setting $(I_{ROB} − I_{BG})/(I_{REF} − I_{BG})$ after bleaching to 0.

Assembly of protein cage-stabilized protein condensates

For sequential cage stabilization, protein condensates were formed for 2 min under given conditions (e.g., [PSH]/[Ni^{2+}]: 50/50 μM, [PS-RL48]/[Ni^{2+}]: 30/30 μM, [LAF] / [Ni^{2+}]: 20/20 μM, [PS2H]/[NaCl]: 50 μM/60 mM), followed by the addition of various protein cages (final concentrations: 50 μg/mL). For one-pot assembly of protein cage-stabilized condensates, $NiCl_2$ was introduced (or mixing NaCl-free phosphate buffer for PS2H) to scaffold/cage mixtures to induce LLPS. Assembly procedures were optimized by adjusting total protein concentrations, scaffold/cage ratios, crowding agent PEG 8000 (LPS solution), salt concentrations, and applied protein cages. To measure

condensate formation yields, assembled condensates were centrifuged at 14,000 × g for 30 min. The resulting condensate pellets were resuspended and applied to 15% SDS-PAGE denaturing gels. Gels were stained with Coomassie Blue and imaged by ChemiDoc MP (Biorad).

Total condensate surface area and interfacial cages density calculation

Assumptions were made that the condensates are spherical and that all cage and scaffold proteins were assembled into the condensates. From the confocal images, the average cross-sectional area (A) of the condensates was calculated. The average radius (r) was then determined using the equation $r = \sqrt{A/\pi}$. The average volume (V) of the condensates was calculated based on the average radius using ($V = \frac{4}{3}\pi r^3$). The total volume of the condensates within a 1 nL solution was determined based on the initial scaffold concentration and the scaffold concentration within the condensate phase[30] after LLPS. The total volume (x) was determined as: $x = $ unit volume $\times \frac{initial\ scaffold\ concentration}{condensate\ internal\ concentration}$. Next, the total number of condensates in the 1 nL solution was calculated as: Number $= \frac{total\ volume}{average\ volume} = \frac{x}{\frac{4}{3}\pi r^3}$. Using these formulas, the total surface area of the condensates in the solution was determined as: total surface area $= $ Number $\times 4\pi r^2 = \frac{3x}{r}$. Finally, the surface density of cages was calculated as: Surface density $= \frac{Cage\ molarity \times Avogadro's\ number}{total\ surface\ area} = (cage\ molarity \times 6.02 \times 10^{23}) \times \frac{r}{3x}$.

Interfacial tension measurement

The interfacial tension of the condensates was calculated using the equation $\tau \approx \ell(\eta/\gamma)$[26]. Time-lapse movies of both uncaged and caged PSH condensates were used to observe their coalescence. The relaxation time (τ) was determined by measuring the duration it takes for two neighboring condensates to collide and fuse into a single entity. The length scale (ℓ) of the condensates was calculated as the geometric mean of the two fusing condensates. Plotting τ against ℓ produced a line, with the slope representing the ratio of viscosity (η) to surface tension (γ).

Negative-stained transmission electron microscopy (TEM)

Cage protein samples (0.03 mg/mL) were adsorbed on a glow-discharged carbon-coated grid (200 mesh, TED PELLA, INC) for 2 min. Condensate samples were used as assembled without dilution. The grid was washed with distilled water twice. To achieve negative staining, the grid was treated with 2% uranyl acetate for 1 min and then air-dried for 10 min. The samples were examined using a Tecnai G2 F30 S-Twin 300 kV TEM. Images were acquired at various magnifications (×2900, ×3900, ×5000, ×25,000, or ×35,000), depending on sample sizes.

Size distribution analysis

Size distribution curves were fitted using Origin employing statistics from condensates acquired in TEM or confocal images. Images were converted to binary format using the ImageJ software, and assuming that the condensates are circular, the diameters were computed by inverting the area.

Cryo-EM/ET sample preparation

Quantifoil Cu 400-mesh R1.2/1.3 holey carbon grids (Quantifoil Micro Tools GmbH, Germany) were glow-discharged (0.38 mbar/15 mA/30 s). Grids were then loaded with 3–4 μL of condensate sample solution, blotted, and plunge-frozen in liquid ethane using Vitrobot (Thermo Fisher Scientific, USA). For certain LAF-associated condensate samples, 10 nm BSA-treated gold nanoparticles were introduced as a fiducial marker. Grids were then stored in liquid nitrogen until they were imaged.

Cryo-electron tomography (cryo-ET) and tomogram reconstruction

Vitrified sample grids were loaded onto either Titan Krios (300 kV) or Titan Glacios (200 kV) TEM (Thermo Fisher Scientific, USA). The tilt series were acquired using Tomography software (Thermo Fisher Scientific, USA). The tilt series were acquired over a tilt range of −60° to 60° with an increment of 2°, while limiting the total cumulative electron dose under 120e/Å^2 [50]. Nominal magnification was 53 k× with a pixel size of 0.24 nm. Tilt series images were aligned and reconstructed using IMOD[51,52]. With samples containing gold fiducial markers, cross-correlation and fiducial marker tracking were used to align the tilt series. For samples without gold fiducial markers, on the other hand, cross-correlation and patch-tracking were used in an alignment process. Aligned tilt series were then used to reconstruct tomograms. All tomograms were reconstructed with the SIRT (Simultaneous Iterative Reconstruction Technique) algorithm[51,52], with an iteration number of 20.

For visual representation, image filters were applied using ImageJ software[53]. The segmentation process was done using the 3dmod software in an IMOD package. Tomogram images were pre-processed using filters such as Gaussian blur prior to segmentation. The location of surface cages (GFP-fused mi3) was manually determined to build 3D volume models. Cages were visualized as 25 nm spheres (the size of mi3), since GFPs fused on mi3 were not clearly observed in cryo-EM images. Spherical cage structures with matching diameters (in both the XY and Z directions on the tomogram) and significantly higher density compared to the surrounding area were identified as mi3 cages. Since the sample typically consists of only two protein components, a 25 nm cage structure is sufficient to determine the basic location of the cage. The trainable Weka Segmentation 3D software[54] was used to further validate the manual segmentation. Using several manually selected mi3 cage structures as training input, the Weka software scanned the entire tomogram and identified pixels with a high probability of belonging to mi3 entities. The manual segmentation was validated by ensuring that no significant discrepancies existed between the manual and Weka segmentation results. Contact angles were measured by drawing a line connecting two intersection points at the contact site of mi3 on a condensate surface and another line, tangential to the cage circle at these intersection points. Note that measured contact angles might have been understated, since GFP-fused mi3 is probably larger than 25 nm.

Client recruitment

mCherry-6His (2 μM) and Cy5-DNA (25 nM) (300–1000 bp) were treated to pre-formed cage-stabilized condensates. For one-pot recruitment, these biomolecules were mixed together with scaffolds and protein cages prior to Ni^{2+}-induced LLPS. For recruiting Human IgG (Sigma), a mixture of 48 μM of PSH and 2 μM of Protein G-PSH were used as scaffold proteins. Scaffolds, 0.1 μM of Cy5-tagged HIgG, and HF oligo mixtures were incubated for 5 min before Ni^{2+}-triggered LLPS. Encapsulation efficacies were investigated by gel electrophoresis, where condensates (pellets) and non-participants (supernatants) were separated through centrifugation (at $14,000 \times g$ for 30 min), then loaded onto denaturing gels. Fluorescence signals of DNA and IgG were investigated by ChemiDoc MP (Biorad).

Sucrose density gradient centrifugation

Sucrose solutions were prepared in 10% increments, ranging from 10% to 60%. A discontinuous sucrose gradient column was built up in polypropylene tubes (Beckman), with 2 mL of each sucrose solution layered from bottom to top, followed by 1 mL of cage-stabilized protein condensate mixtures transferred to the highest layer of the sucrose gradient column. Samples were centrifuged (Optima XE-90, Beckman) at 20,000×g for 20 min at 4 °C using the SW41Ti rotor. Afterward, a 1 mL aliquot was carefully isolated from the top layer of the gradient.

Cell experiments

HeLa (ATCC, CCL-2) and U2OS (ATCC, HTB-96) cells were cultured in Dulbecco's Modified Eagle's Medium (DMEM, Gibco) supplemented with 10% fetal bovine serum (HyClone) and 1% penicillin/streptomycin. Cells were seeded in 8-well plates (ibidi) at a density of 1×10^4 cells per well and incubated at 37 °C with 5% CO_2 in a humidified atmosphere for 24 h. Following incubation, the DMEM was removed and the cells were washed twice with cold Dulbecco's phosphate-buffered saline (DPBS) before being treated with various condensates. Cells were treated with condensates at 37 °C for 30 min to 2 h, washed twice with cold DPBS, and then incubated at 37 °C for 1 h to 24 h, depending on experimental conditions. Fluorescent images of HeLa and U2OS cells were acquired using a confocal microscope. Nuclei were labeled with DAPI (Vector Labs). For time-lapse imaging analysis (e.g., fusion or FRAP), observations were made without nuclei staining. For FRAP experiments in cells, the imaging interval was shortened to 0.6 s (the minimal limit), and image resolution was dropped from 1024×1024 pixels to 512×512 pixels to capture rapid fluorescence recovery. The cytotoxicity of free scaffolds and condensates was evaluated using the Quanti-Max™ WST-8 cell viability assay (Biomax) in HeLa cells. Cells were seeded into 96-well plates at a density of 1×10^4 cells each and incubated for 24 h. After 30 min of treating cells with various protein samples, the media was replaced with serum-free DMEM. Following an additional 24 h incubation at 37 °C, cells were treated with Quanti-Max™ solution and incubated for 1 h. Absorbance was measured at 450 nm using a Varioskan Flash microplate spectrofluorometer (Thermo Scientific). Cell viability was expressed as a percentage relative to untreated control cells, which were considered to have 100% viability.

Statistics and reproducibility

All statistical values provided are represented as mean ± 0.5 standard deviation, with the number of samples (n) indicated. Confocal, TEM, and ET micrographs, as well as gel images, were consistent across at least three independently conducted experiments.

Reporting summary

Further information on research design is available in the Nature Portfolio Reporting Summary linked to this article.

Data availability

Cryo-EM data were deposited in EMPIAR (Electron Microscopy Public Image Archive) (mi3-stabilized LAF condensates: deposition ID 47486196, public accession code EMPIAR-12294; mi3-stabilized PSH condensates: deposition ID 47486195, public accession code EMPIAR-12295). All data supporting the results of this study can be found in the article, supplementary, and source data files. Source data are provided with this paper.

References

1. Brangwynne, C. P., Tompa, P. & Pappu, R. V. Polymer physics of intracellular phase transitions. *Nat. Phys.* **11**, 899–904 (2015).
2. Shin, Y. & Brangwynne, C. P. Liquid phase condensation in cell physiology and disease. *Science* **357**, eaaf4382 (2017).
3. Banani, S. F., Lee, H. O., Hyman, A. A. & Rosen, M. K. Biomolecular condensates: organizers of cellular biochemistry. *Nat. Rev. Mol. Cell Biol.* **18**, 285–298 (2017).
4. Alberti, S., Gladfelter, A. & Mittag, T. Considerations and challenges in studying liquid-liquid phase separation and biomolecular condensates. *Cell* **176**, 419–434 (2019).
5. Boeynaems, S. et al. Protein phase separation: a new phase in cell biology. *Trends Cell Biol.* **28**, 420–435 (2018).
6. Alberti, S. Phase separation in biology. *Curr. Biol.* **27**, R1097–R1102 (2017).

7. Ma, Q. et al. Cell-inspired all-aqueous microfluidics: from intracellular liquid-liquid phase separation toward advanced biomaterials. *Adv. Sci.* **7**, 1903359 (2020).

8. Villegas, J. A., Heidenreich, M. & Levy, E. D. Molecular and environmental determinants of biomolecular condensate formation. *Nat. Chem. Biol.* **18**, 1319–1329 (2022).

9. Abbas, M., Lipinski, W. P., Wang, J. & Spruijt, E. Peptide-based coacervates as biomimetic protocells. *Chem. Soc. Rev.* **50**, 3690–3705 (2021).

10. Son, J. & Jung, Y. Lipid coated protein condensates as stable protocells with selective uptake abilities for biomolecules. *Chem. Sci.* **13**, 11841–11848 (2022).

11. Iwata, T. et al. Liquid droplet formation and facile cytosolic translocation of IgG in the presence of attenuated cationic amphiphilic lytic peptides. *Angew. Chem. Int. Ed.* **60**, 19804–19812 (2021).

12. Sun, Y. et al. Phase-separating peptides for direct cytosolic delivery and redox-activated release of macromolecular therapeutics. *Nat. Chem.* **14**, 274–283 (2022).

13. Peeples, W. & Rosen, M. K. Mechanistic dissection of increased enzymatic rate in a phase-separated compartment. *Nat. Chem. Biol.* **17**, 693–702 (2021).

14. Liu, J., Zhorabek, F., Dai, X., Huang, J. & Chau, Y. Minimalist design of an intrinsically disordered protein-mimicking scaffold for an artificial membraneless organelle. *ACS Cent. Sci.* **8**, 493–500 (2022).

15. Le Ferrand, H., Duchamp, M., Gabryelczyk, B., Cai, H. & Miserez, A. Time-resolved observations of liquid-liquid phase separation at the nanoscale using in situ liquid transmission electron microscopy. *J. Am. Chem. Soc.* **141**, 7202–7210 (2019).

16. Ranganathan, S. & Shakhnovich, E. I. Dynamic metastable long-living droplets formed by sticker-spacer proteins. *Elife* **9**, e56159 (2020).

17. Heuer-Jungemann, A. et al. The role of ligands in the chemical synthesis and applications of inorganic nanoparticles. *Chem. Rev.* **119**, 4819–4880 (2019).

18. McClements, D. J. & Jafari, S. M. Improving emulsion formation, stability and performance using mixed emulsifiers: a review. *Adv. Colloid Interface Sci.* **251**, 55–79 (2018).

19. De, S., Malik, S., Ghosh, A., Sahab, R. & Saha, B. A review on natural surfactants. *RSC Adv.* **5**, 65757–65767 (2015).

20. Kelley, F. M., Favetta, B., Regy, R. M., Mittal, J. & Schuster, B. S. Amphiphilic proteins coassemble into multiphasic condensates and act as biomolecular surfactants. *Proc. Natl. Acad. Sci. USA* **118**, e2109967118 (2021).

21. Linsenmeier, M. et al. The interface of condensates of the hnRNPA1 low-complexity domain promotes formation of amyloid fibrils. *Nat. Chem.* **15**, 1340–1349 (2023).

22. Albert, C. et al. Pickering emulsions: preparation processes, key parameters governing their properties and potential for pharmaceutical applications. *J. Control. Release* **309**, 302–332 (2019).

23. Yang, Y. et al. An overview of Pickering emulsions: solid-particle materials, classification, morphology, and applications. *Front Pharmacol.* **8**, 287 (2017).

24. Xiao, M., Xu, A., Zhang, T. & Hong, L. Tailoring the wettability of colloidal particles for Pickering Emulsions via surface modification and roughness. *Front. Chem.* **6**, 225 (2018).

25. Gonzalez Ortiz, D., Pochat-Bohatier, C., Cambedouzou, J., Bechelany, M. & Miele, P. Current trends in pickering emulsions: particle morphology and applications. *Engineering* **6**, 468–482 (2020).

26. Folkmann, A. W., Putnam, A., Lee, C. F. & Seydoux, G. Regulation of biomolecular condensates by interfacial protein clusters. *Science* **373**, 1218–1224 (2021).

27. Cochard, A. et al. RNA at the surface of phase-separated condensates impacts their size and number. *Biophys. J.* **121**, 1675–1690 (2022).

28. Binks, B. P. Particles as surfactants—similarities and differences. *Curr. Opin. Colloid Interface Sci.* **7**, 21–41 (2002).

29. Levine, S., Bowen, B. D. & Partridge, S. J. Stabilization of emulsions by fine particles II. capillary and van der Waals forces between particles. *Colloids Surf.* **38**, 345–364 (1989).

30. Hong, K., Song, D. & Jung, Y. Behavior control of membrane-less protein liquid condensates with metal ion-induced phase separation. *Nat. Commun.* **11**, 5554 (2020).

31. Valenti, L. E., De Pauli, C. P. & Giacomelli, C. E. The binding of Ni(II) ions to hexahistidine as a model system of the interaction between nickel and His-tagged proteins. *J. Inorg. Biochem.* **100**, 192–200 (2006).

32. Jozic, D., Kaiser, J. T., Huber, R., Bode, W. & Maskos, K. X-ray structure of isoaspartyl dipeptidase from E.coli: a dinuclear zinc peptidase evolved from amidohydrolases. *J. Mol. Biol.* **332**, 243–256 (2003).

33. Jutz, G., van Rijn, P., Santos Miranda, B. & Boker, A. Ferritin: a versatile building block for bionanotechnology. *Chem. Rev.* **115**, 1653–1701 (2015).

34. Hsia, Y. et al. Design of a hyperstable 60-subunit protein dodecahedron. [corrected].*Nature* **535**, 136–139 (2016).

35. Oh, H. J. & Jung, Y. High order assembly of multiple protein cages with homogeneous sizes and shapes via limited cage surface engineering. *Chem. Sci.* **14**, 1105–1113 (2023).

36. Kunzle, M., Eckert, T. & Beck, T. Binary protein crystals for the assembly of inorganic nanoparticle superlattices. *J. Am. Chem. Soc.* **138**, 12731–12734 (2016).

37. Rivas, G. & Minton, A. P. Macromolecular crowding in vitro, in vivo, and in between. *Trends Biochem. Sci.* **41**, 970–981 (2016).

38. Abyzov, A., Blackledge, M. & Zweckstetter, M. Conformational dynamics of intrinsically disordered proteins regulate biomolecular condensate chemistry. *Chem. Rev.* **122**, 6719–6748 (2022).

39. Elbaum-Garfinkle, S. et al. The disordered P granule protein LAF-1 drives phase separation into droplets with tunable viscosity and dynamics. *Proc. Natl. Acad. Sci. USA* **112**, 7189–7194 (2015).

40. Saibil, H. R. Cryo-EM in molecular and cellular biology. *Mol. Cell.* **82**, 274–284 (2022).

41. Liu, N. & Wang, H. W. Better Cryo-EM specimen preparation: how to deal with the air–water interface? *J. Mol. Biol.* **435**, 167926 (2023).

42. Wang, J., Devarajan, D. S., Nikoubashman, A. & Mittal, J. Conformational properties of polymers at droplet interfaces as model systems for disordered proteins. *ACS Macro Lett.* **12**, 1472–1478 (2023).

43. Lisuzzo, L., Hueckel, T., Cavallaro, G., Sacanna, S. & Lazzara, G. Pickering Emulsions based on wax and halloysite nanotubes: an ecofriendly protocol for the treatment of archeological woods. *ACS Appl. Mater. Interfaces* **13**, 1651–1661 (2021).

44. Sjöbring, U., Björck, L. & Kastern, W. Streptococcal protein G. Gene structure and protein binding properties. *J. Biol. Chem.* **266**, 399–405 (1991).

45. Bao, Y. et al. Photo-responsive phase-separating fluorescent molecules for intracellular protein delivery. *Angew. Chem. Int. Ed.* **62**, e202307045 (2023).

46. Garcia-Jove Navarro, M. et al. RNA is a critical element for the sizing and the composition of phase-separated RNA-protein condensates. *Nat. Commun.* **10**, 3230 (2019).

47. Hampoelz, B. et al. Nuclear pores assemble from nucleoporin condensates during oogenesis. *Cell* **179**, 671–686 (2019).

48. Tauber, D. et al. Modulation of RNA condensation by the DEAD-Box Protein eIF4A. *Cell* **180**, 411–426 (2020).

49. Dekker, R. I. et al. Is there a difference between surfactant-stabilised and Pickering emulsions? *Soft Matter* **19**, 1941–1951 (2023).

50. Tollervey, F. et al. Cryo-electron tomography of reconstituted biomolecular condensates. *Methods Mol. Biol.* **2563**, 297–324 (2023).

51. Kremer, J. R., Mastronarde, D. N. & McIntosh, J. R. Computer visualization of three-dimensional image data using IMOD. *J. Struct. Biol.* **116**, 71–76 (1996).
52. Mastronarde, D. N. & Held, S. R. Automated tilt series alignment and tomographic reconstruction in IMOD. *J. Struct. Biol.* **197**, 102–113 (2017).
53. Schindelin, J. et al. Fiji: an open-source platform for biological-image analysis. *Nat. Methods* **9**, 676–682 (2012).
54. Arganda-Carreras, I. et al. Trainable Weka Segmentation: a machine learning tool for microscopy pixel classification. *Bioinformatics* **33**, 2424–2426 (2017).

Acknowledgements

Author contributions

H.J.O. and Y.L. designed, conducted and analyzed experiments. H.H. and J.Y.K. helped structural analysis using cryo-EM and -ET. K.H. and H.C. initiated the project. Y.J., H.J.O., and Y.L. wrote the manuscript with help from all authors. Y.J. designed the project and supervised the work.

Competing interests

The authors declare no competing interests.

Additional information

Supplementary information The online version contains supplementary material available at https://doi.org/10.1038/s41467-025-56391-y.

Correspondence and requests for materials should be addressed to Yongwon Jung.

Peer review information *Nature Communications* thanks Yusuke Sato and the other, anonymous, reviewer(s) for their contribution to the peer review of this work. A peer review file is available.

Reprints and permissions information is available at http://www.nature.com/reprints

Publisher's note Springer Nature remains neutral with regard to jurisdictional claims in published maps and institutional affiliations.